Electronic Supplementary Material (ESI) for Green Chemistry.

Supplementary Information

Dual Functionality of Mixed Cu-based Two-Dimensional (2D) Heterostructures Derived from Electronic Wastes

Rasoul Khayyam Nekouei[1,2,3,*], Ignacio Tudela[2], Sajjad S. Mofarah[1], Ehsan Vahidi[4], Samane Maroufi[1], Ke Wang[2], Farshid Pahlevani[1], Veena Sahajwalla[1,*]

[1] Centre for Sustainable Materials Research and Technology, SMaRT@UNSW, School of Materials Science and Engineering, UNSW Sydney, NSW 2052, Australia

[2] School of Engineering, The University of Edinburgh, Edinburgh, EH9 3FB, United Kingdom

[3] Department of Materials Science and Engineering, Massachusetts Institute of Technology (MIT), Cambridge, MA, 02139, United States of America (USA)

[4] Department of Mining and Metallurgical Engineering, Mackay School of Earth Sciences and Engineering, University of Nevada, Reno, NV 89557, United States of America (USA)

***Corresponding author: r.nekouei@unsw.edu.au; rnekouei@mit.edu**

Table of contents

SUPPLEMENTARY NOTE 1 | ELECTROCHEMICAL ANALYSIS

The reason why -1.5 V *vs*. Ag/AgCl was chosen for the citrate deposition is to maximise the adherence, although even in -1 V Cu could deposit on FTO but can easily be peeled off.

Citrate and nitrate ions are complexing agents for changing the electrodeposition conditions. The effect of citrate ligand ($Cit^{-3} = C_6H_5O_7^{3-}$) has been discussed in the previous studies[1,2]. During the deposition in both bathes, no gas evolution was noticed on WE, proving the high efficiency of electrodeposition. It is claimed that the addition of citrate (more than 0.5 M) increases the current efficiency to more than 100% and also actively suppresses Cu reduction[3]. Subsequently, deposition in citrate bath needed more negative voltage (-1.5V).

In **Fig. S1**, the deposition current *vs.* time is illustrated for both deposition solutions. The slopes of curves prove that in spite of having less conductivity (90 $mS.cm^{-1}$) and more deposition time, the deposition of a homogenous Cu layer is more facile from the citrate solution, whereas the rapid drop in current during the deposition from the nitrate solution, with the conductivity of 110 $mS.cm^{-1}$, might indicate the multiphasic film.

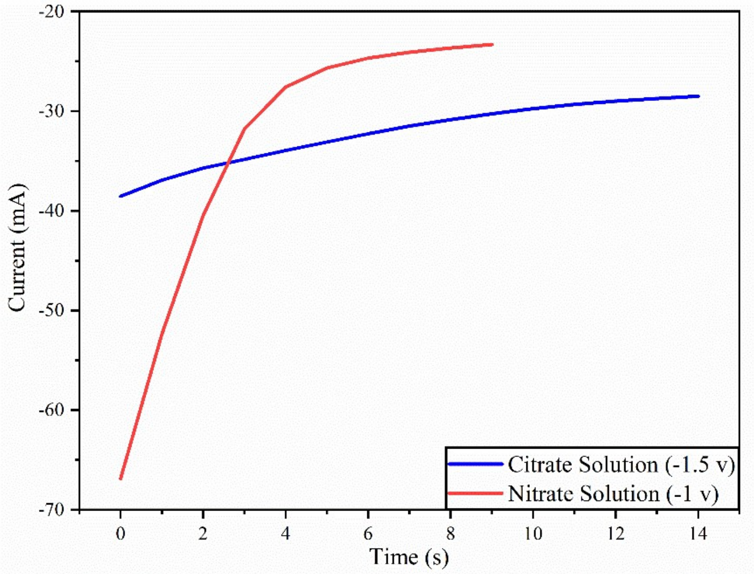

Fig. S1 Chronoamperometery plot of Cu/Cu oxide deposition from the citrate solution (pH ~6.6 and conductivity ~90 $mS.cm^{-1}$) and nitrate solution (pH ~4.8 and conductivity ~110 $mS.cm^{-1}$) under different applied voltages vs. Ag/AgCl.

Cu ions are not stable in citrate media and forms complexes with citrate ions[1]. The cathodic reaction of Cu deposition in the presence of citrate at pH ≈ 6 is[2]:

$$Cu_2Cit_2^{-2} + 4e^- = 2Cu + 2\ Cit^{-3} \qquad \textbf{Re. S1}$$

The deposited Cu film serves as an interlayer for subsequent copper oxide film and supports the electron conductivity of the substrate[4].

$Cu\text{-}OH_{ads}$, at point E in **Fig. 2**d, can be formed due to the abundance of OH^- in the close adjacency of the surface that subsequently is transformed into $CuO/Cu(OH)_2$ [5].

$Cu + OH^- = Cu\text{-}OH_{ads} + e^-$ [5] **Re. S2**

$Cu\text{-}OH_{ads} + OH^- = Cu(OH)_2$ [5] **Re. S3**

As shown in **Fig. 2**d, the presence of $Cu(OH)_2$ in the film deposited from the nitrate bath was confirmed visually with the black-bluish surface[5] of the film.

SUPPLEMENTARY NOTE 2 | FILM CHARACTERISATION

In **Fig. S2**, XRD patterns of FTO and heat-treated FTO substrate (as standard sample) are illustrated.

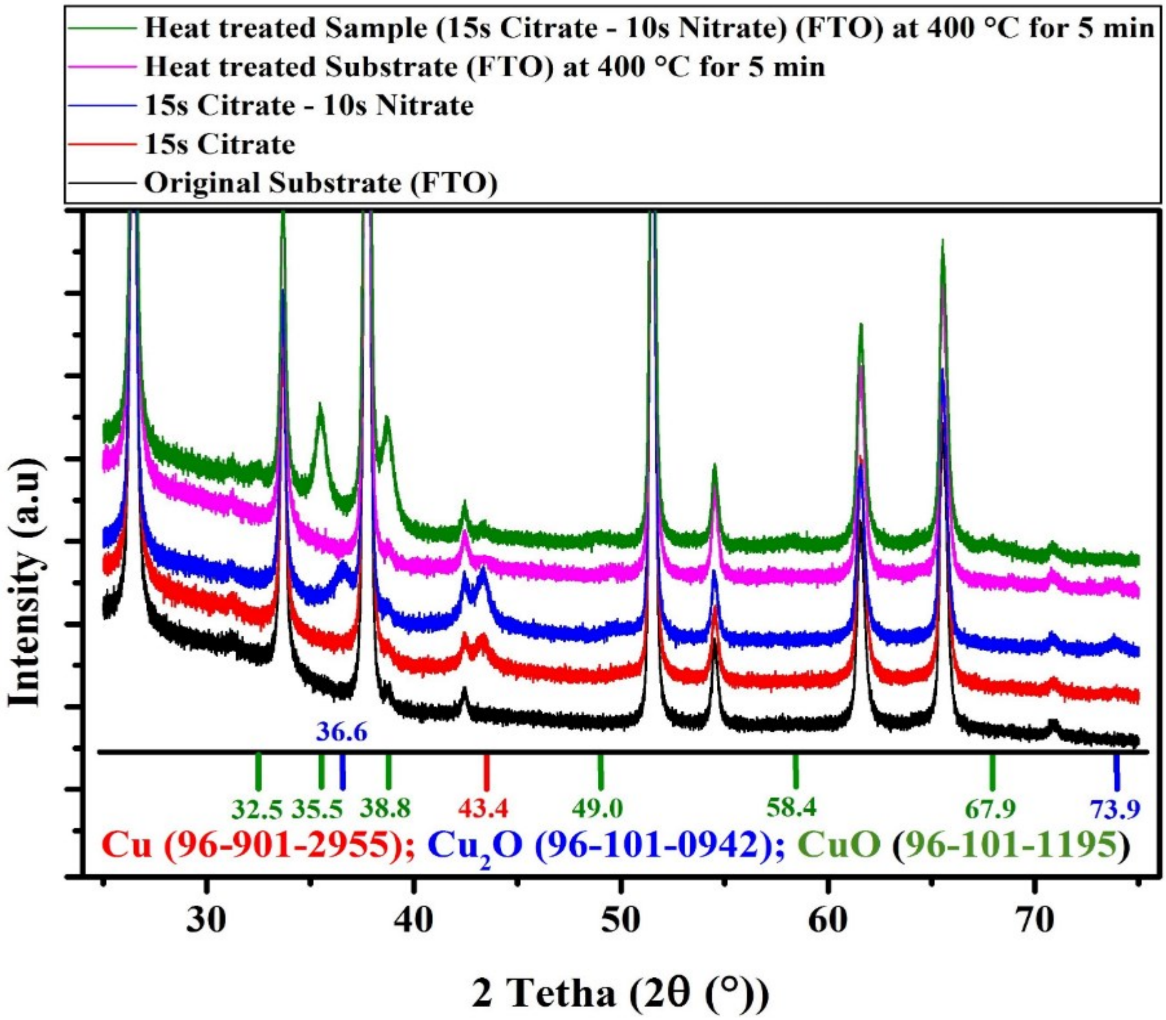

Fig. S2 XRD patterns of the samples and analysed results. Peaks in 32.5, 35.5, 38.8, 49.0, 58.4, and 67.9°, respectively, represent planes (110), (11-1), (111), (20-2), (202), and (113) for CuO with monoclinic structure. Peaks in 36.6 and 73.9°, respectively, represent plans (111) and (113) for Cu_2O with cubic structure. The peak in 43.4° represents plans (111) for Cu with cubic structure.[6]

In **Fig. S3**, the black shapes inside the films are supposedly voids due to scattering almost no electron toward the SEM detector[7]. Regarding the fact that the density of Cu, Cu_2O, and CuO, respectively, are 8.96, 6.0, and 6.3 $g.cm^{-3}$, it makes sense that the transformation of Cu-Cu_2O to CuO accompanies with leaving interconnected porosity. As a matter of fact, this higher level of connected porosity can help the penetration of electrolyte into the film structure[8].

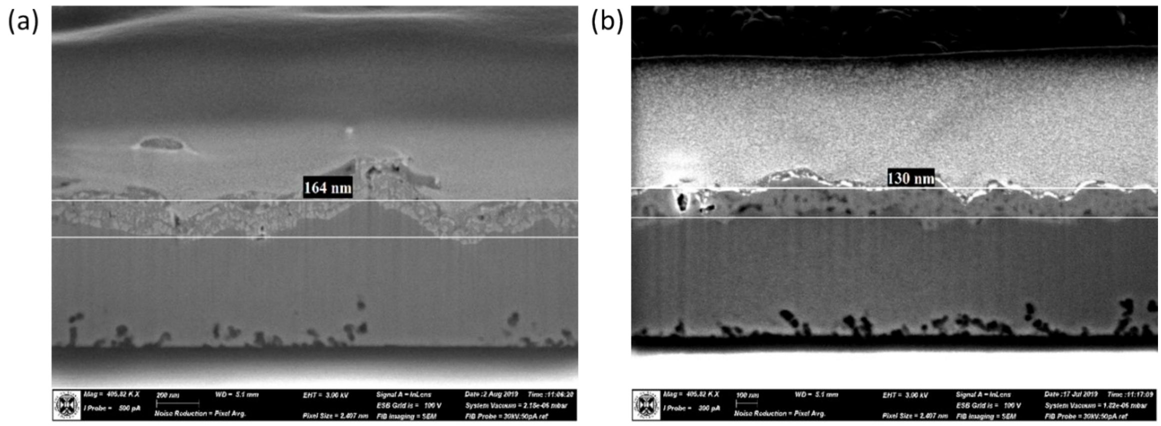

Fig. S3 FE-SEM images from the cross-section of **(a)** the as-deposited film after two steps of electrodeposition, and **(b)** the deposited film after the thermal processing at 400°C for 5 min.

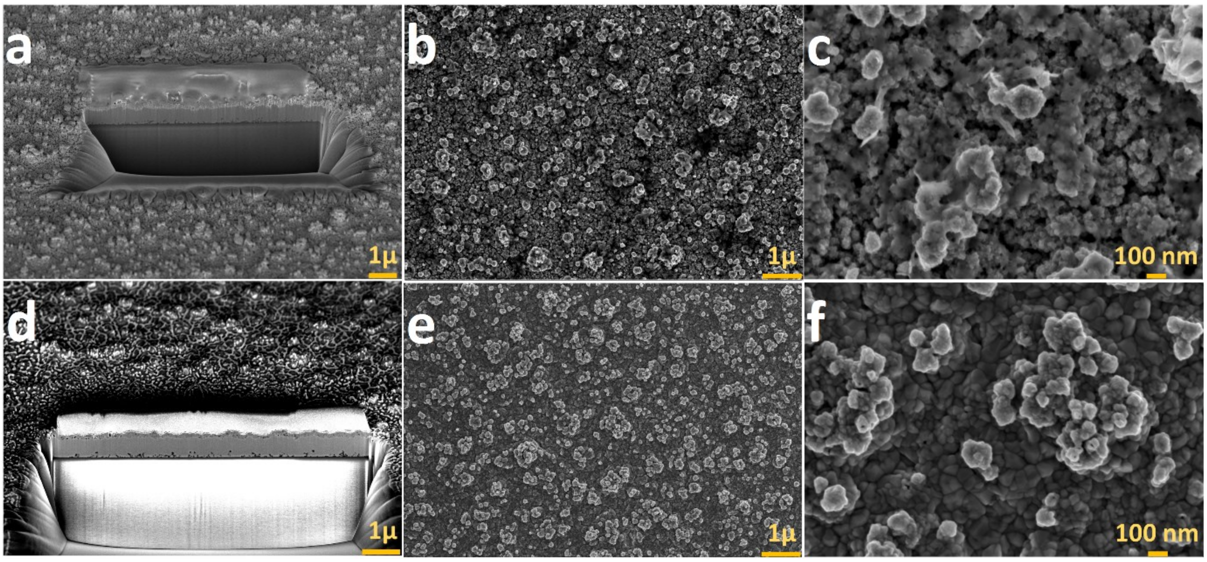

Fig. S4 **(a)** Cross-section of the FIB-SEM, and **(b-C)** FE-SEM of the top view of the ultra-thin film after electrodeposition (before heat treatment); **(d)** cross-section of the FIB-SEM, and **(e-f)** FE-SEM of the top view of the ultra-thin film after heat treatment.

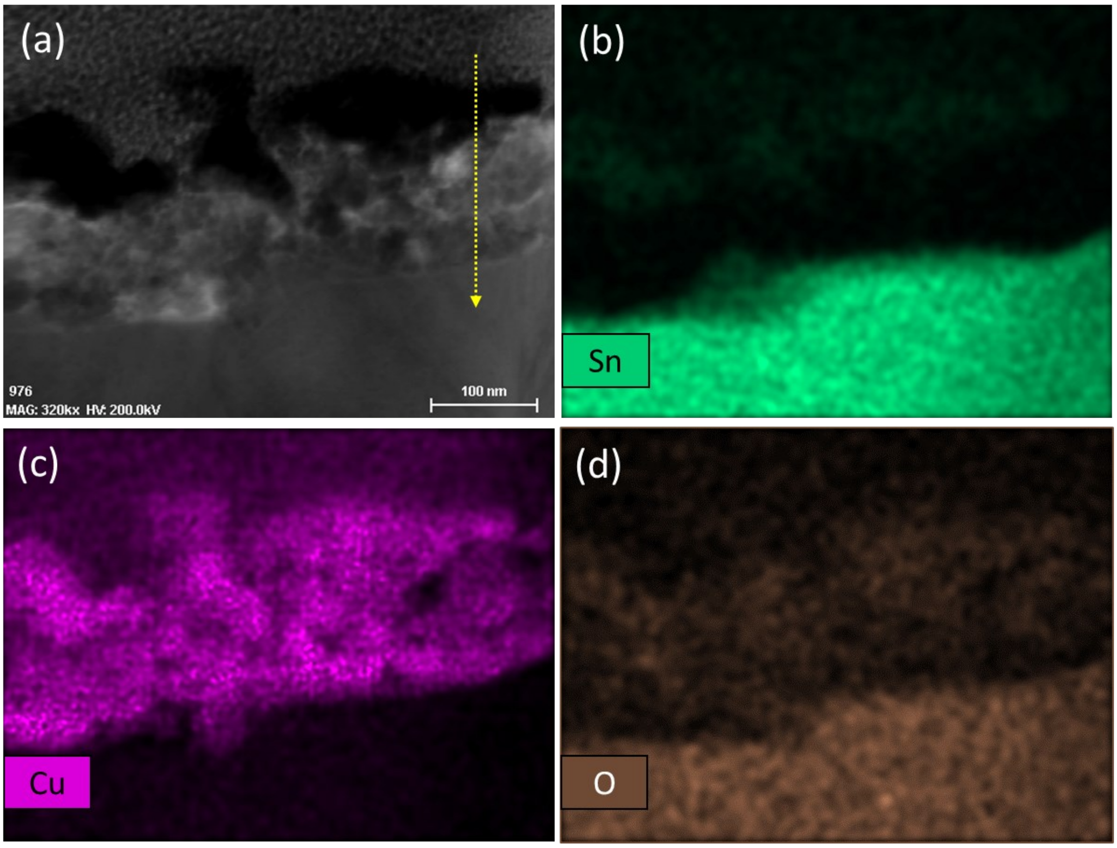

Fig. S5 **(a)** HT-TEM image and **(b-d)** EDS mapping of the trilayer Cu-based film for (b) Sn, (c) Cu, and (d) O elements. The yellow arrow in (a) represents the line scanning profile shown in **Fig. 3**c in the main draft.

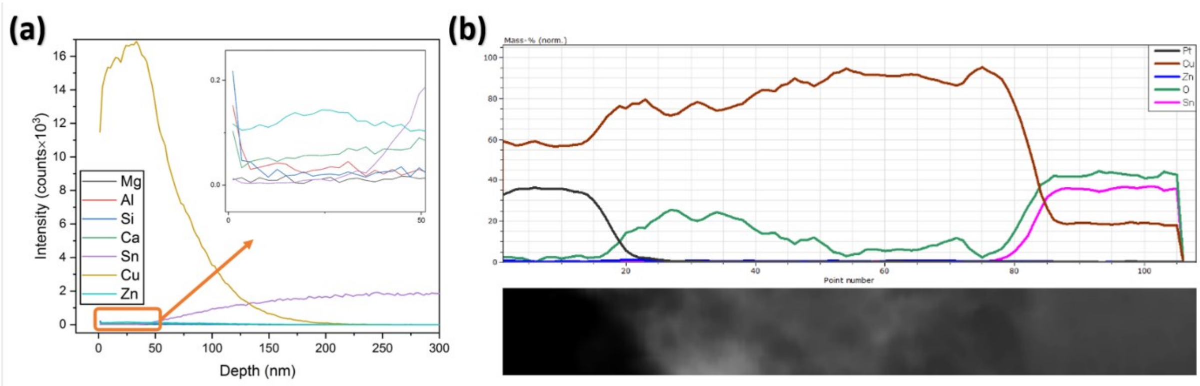

Fig. S6 **(a)** TOF-SIMS analysis showing the concentration of elements *vs.* the penetration depth from the surface, and **(b)** EDS line profile of trilayer Cu-based ultrathin film deposited in citrate media (first step of deposition).

As shown in **Fig. S7**, HRTEM image of the bilayer Cu-based ultrathin film shows a polycrystalline structure with randomly oriented nanocrystallites. The d-space of a selected area, as shown in **Fig. S7**a, was measured to be 0.247 nm using d-space profile illustrated in **Fig. S7**b. Further, fast-fourier transform (FFT) analysis from the HRTEM image (**Fig. S7**c) revealed dots with the reciprocal length of 4.01 1/nm, which is equivalent to the d-space of

0.249 nm, in consistent with that of presented in **Fig. S7**b. The d-space of 0.249 nm is associated with the 2ϴ = 35.97° that can be ascribed to the (111) plane of Cu_2O structure. However, the measured 2ϴ value revealed a shift towards lower degrees with respect to the one for pristine Cu_2O, which is positioned at 36.6°. This indicates an expansion of d-space and thus the crystal structure, that is a well-known phenomenon mainly owing to the presence of defects in the structure[9,10].

Similarly, the trilayer Cu-based ultrathin film obtained after heat treatment at 400°C revealed both expansion and contraction in the lattice fringes. **Fig. S7**e shows a representative d-space profile with the value of 0.256 nm. The FFT results, as shown in **Fig. S7**f, illustrate two sets of dots, as highlighted with purple and blue colours. The dots enclosed by blue circles are ascribed to the (11-1) plane (d-space = 0.256 nm) of CuO structure with 2ϴ = 34.9° and the dots with magenta circles show (111) plane (d-space = 0.227 nm) of CuO structure with 2ϴ = 39.6°. The former shows expansion respect to the (11-1) plane of pristine CuO structure with 2ϴ = 35.5°, while the latter demonstrates contraction respect to the (111) plane of pristine CuO structure with 2ϴ = 38.8°. Such significant changes, shown by both d-space profile and FFT pattern, in the d-space values, clearly indicate the presence of structural defects created as a result of Cu and oxygen vacancies[11].

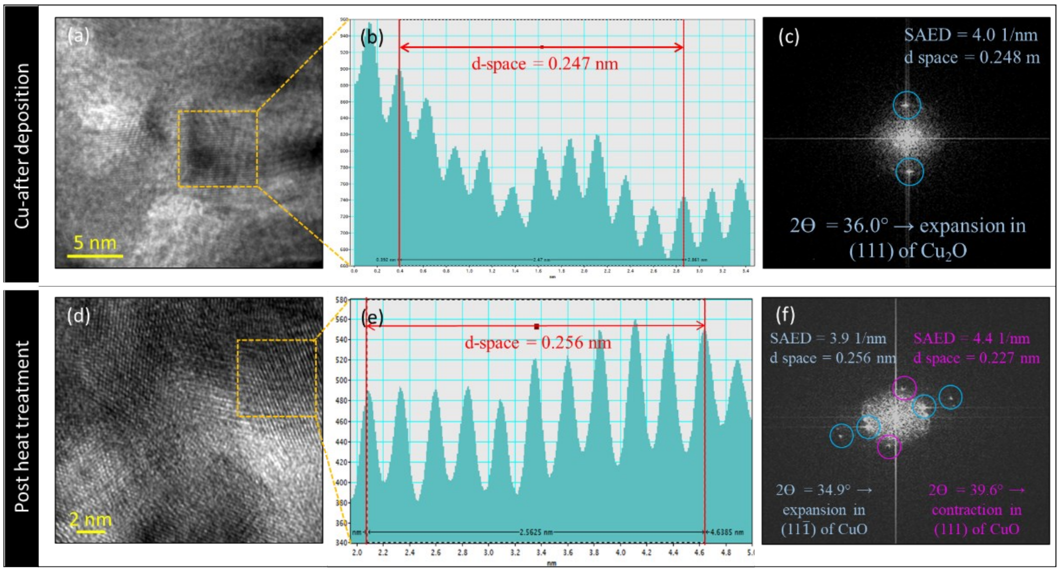

Fig. S7 **(a)** HRTEM image of Cu-based ultrathin film after deposition; **(b)** d-space profile derived from the dotted square shown in (a); **(c)** fast fourier transform (FFT) pattern obtained from HRTEM image shown in (a); **(d)** HRTEM image of Cu-based ultrathin film after heat treatment at 400°C; **(e)** d-space profile derived from the dotted square shown in (d); **(f)** fast fourier transform (FFT) pattern obtained from HRTEM image shown in (d).

Additional TEM analysis illustrates the highly-defective structure of trilayer Cu-based ultrathin film. **Fig. S8** shows two types of structural faults. The fringes shown within the orange rectangle is ascribed to 1D defects that are formed as a result of either twinning (typically occurs on (110) planes of monoclinic structures[12]) or superlattice structure. The formation of such defects has been extensively studied in the previous literature[13–15]. Moreover, the regions encompassed by red rectangles show the interfacial regions between two or more nanocrystallites, where the mismatch angles resulted in the formation of point (0D) defects. In the field of functional materials for energy and catalysis applications, the formation of structural defects is considered as the generation of active sites to enhance the performance of capacitors and/or catalysts[11,16,17].

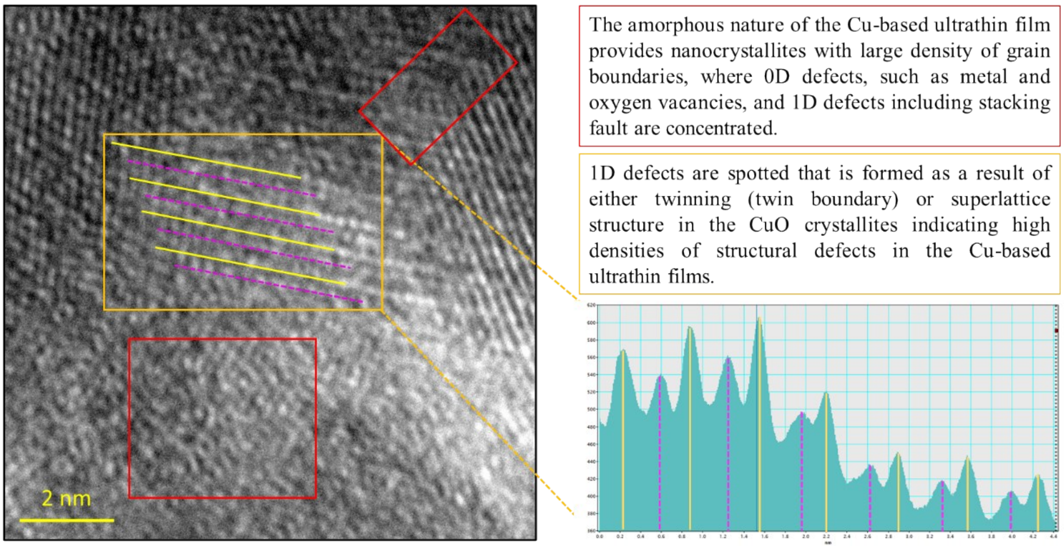

The amorphous nature of the Cu-based ultrathin film provides nanocrystallites with large density of grain boundaries, where 0D defects, such as metal and oxygen vacancies, and 1D defects including stacking fault are concentrated.

1D defects are spotted that is formed as a result of either twinning (twin boundary) or superlattice structure in the CuO crystallites indicating high densities of structural defects in the Cu-based ultrathin films.

Fig. S8 **(a)** HRTEM image of Cu-based ultrathin film after heat treatment at 400°C, where some representative 0D and 1D structural defects are shown.

A standard method to measure the optical band gap of thin films is the Kubelka-Munk equation. **Fig. S9**a shows the UV-Vis spectra of both film samples before and after heat treatment. **Fig. S9**b is the UV-Vis data after applying the Kubelca-Munk function, in which the extrapolation of plots leads to measuring the direct (allowed) bandgap of semiconductors[18]. As proved, the as-deposited sample contains a $Cu_2O/Cu(OH)_2$ layer on top of a Cu layer, while in the after thermal processing film, both layers transformed significantly into CuO film and there is a thin Cu_2O layer between CuO and Cu layers. Details of Kubelka-Munk method to measure optical bandgap of thin films are comprehensively described in Chapter 5 of ref.[18] and ref.[19].

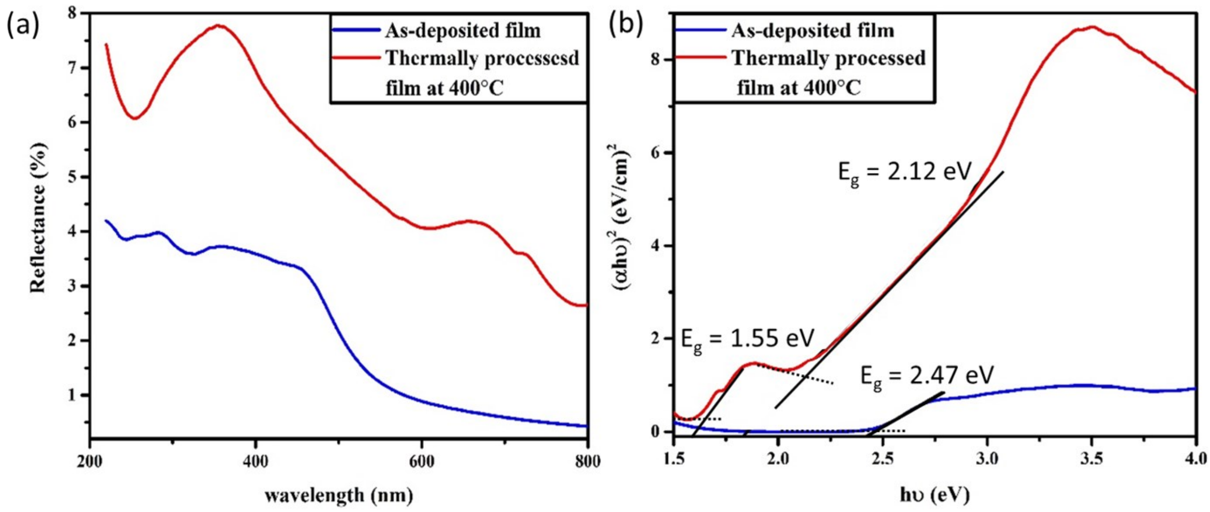

Fig. S9 **(a)** UV-Vis spectra (DRS method) of samples between the wavelength of 200 to 800 nm, and **(b)** the Tauc plot for the bandgap of both samples.

SUPPLEMENTARY NOTE 3 | APPLICATION PERFORMANCE

(a) Supercapacitance application

Supercapacitors are classified into two categories, including pseudocapacitors and electrical double-layer capacitors (EDLCs)[20]. In EDLCs, the energy originates from the reversible non-Faradic reactions happening at the interface of electrode/electrolyte[20]. Cyclic voltammetry (CV), galvanostatic charge/discharge (GCD), and electrochemical impedance spectroscopy (EIS) methods are three standard and frequent tests to benchmark the efficiency of supercapacitors[21]. In EDLCs, the corresponding cyclic voltammogram is rather rectangular. Regarding the GCD method, an ideal EDL supercapacitor follows a linear symmetric rectangular pattern[21,22].

The Specific capacitance (C_S) of a supercapacitor is the first parameter needed for benchmarking. CV and GCD techniques can independently collect the relevant data to calculate this value. The relevant equations are as following and the last two ones are derived from the first one [21]:

$$General\ C_S = \frac{\Delta Q}{A.\Delta V} \qquad \text{Eq. S1}$$

$$C_S\ for\ CV = \frac{\int_0^{\frac{2V_0}{v}} |i|.dt}{A.2V_0} \qquad \text{Eq. S2}$$

$$C_S\, for\, GCD = \frac{I_{dis}.\Delta t_{V_0 - 2V_0}}{A.(V_0 - V_{IR-drop})} \qquad \text{Eq. S3}$$

Where ΔQ is the passed electrical charge, ΔV is the given voltage changed and equals to $2V_0$ (0 to V_0 and back to 0), A is the surface area of the film, v is the potential scan rate in CV, i is the current in CV, I_{dis} is the constant current while discharging in GCD, Δt is the duration of discharge in GCD, and $V_{IR\text{-}drop}$ is the inevitable dropped potential once the current polarity changes from charging to discharging in GCD[21]. The potential window in this research was -0.05 to -0.6 V vs. Ag/AgCl that beyond these limits, the film was at risk of destroying.

The life span of the supercapacitor can be obtained using capacitance retention rate from GCD test by comparing the capacitance after a specific number of cycles, usually in orders of thousands, with that of the first cycles[21].

(b) Photoelectrochemical energy harvesting application

Flat band potential (E_{fb})

In illuminated open circuit potential (OCP), the photoelectrode has undergone from dark to intense illumination. Under intense illumination, where the potential change is minimal/flattened, the measured potential between the photoelectrode and the reference electrode is approximately the E_{fb} *vs.* reference electrode.

During the illumination, electrons and holes move in opposite directions due to the electric field through the space charge layer. The majority carriers move away and minority carriers move toward the photoelectrode/electrolyte interface, resulting in a shift in OCP. Increasing the light intensity enhances the electric field of the movement of photogenerated carriers. This electric filed consequently can neutralise the electric field of the space charge layer, where the OCP is no longer changing with increasing the illumination intensity[23]. Illuminating the surface of a photocatalyst to measure E_{fb} causes shifting the Fermi level of bulk material toward more anodic potentials for p-type semiconductors, such as Cu oxide, which drives hydrogen evolution reaction (HER). Hence, the shifting direction under OCP under illumination determines the conductivity type, which specifies the polarity of the electrode, as well as the working potential window of the photocatalyst[18].

E_{fb}, conductivity type (negative slope for p-type), and free charge carrier density of the photoelectrode can also be obtained from the M-S method. In Mott-Schottky (M-S) method, which is an EIS method, the capacitance of the space charge layer (C_{sc}) of the semiconductor against applied potential (E) over a range of potential is plotted. The related equation is as follow [18]:

$$\frac{1}{C_{SC}^2} = \frac{2}{\varepsilon_r \varepsilon_0 A^2 e N_{dopant}}(E - E_{fb} - \frac{kT}{e}) \qquad \text{Eq. S4}$$

Where ε_r, ε_0, A, e, N_{dopant}, k, T, and E, respectively, are the relative permittivity of the semiconductor (for Cu_2O and CuO is 7.60 and 10.26, respectively[4,19]), permittivity in vacuum, surface area, charge of an electron, free/majority/acceptor carrier density in p-type semiconductors, Boltzmann constant, temperature, and applied potential.

An ideal equivalent circuit in M-S method is simplified to a resistor (R) and a capacitor (C) in series, where the R is the resistance of the semiconductor bulk and series resistance from electrolyte and wiring, and the C is the capacitance of space charge region (C_{SC}).

Photocurrent diagrams

The photocurrent onset potential and its ability for the generation of photocurrent also can be evaluated using a three-electrode j-V test in the presence and absence of illumination. The potential that minority electron carriers in photocathodes (p-type) drive the HER at the liquid-solid interface is called E_{onset}[18].

After carrying out several three-electrode j-V tests under dark, illumination/light, and interrupted/chopped illumination, the potential range of 0.0 to -0.6 V was chosen to ensure no Faradic reaction happens. The most appropriate scan rate in linear voltammetry also was recognised under 10 $mV.s^{-1}$ to minimise any possible errors in capacitance. The chopping frequency was 0.5 Hz to avoid capacitance charging which results in transient photocurrent behaviour[18].

In **Fig. S10**, the film produced from 15 s deposition from the citrate solution followed by 10 s deposition from the nitrate solution offered the highest photocurrent ratio. Increasing the thickness of the film has two opposite effects. Thicker film enhances the light absorption efficiency but also raises the ohmic resistance[19]; hence, the optimum thickness is somewhere in between.

The j-V plot from three-electrode setup represents the photocurrent of the semiconductor while the Fermi level of the photoelectrode varies to the reference electrode. The j-V characteristics depend only on the nature and performance of the semiconductor[23]. However, for water splitting application, the potential needs to be reported against reversible hydrogen electrode (RHE), which is the thermodynamic water reduction potential at a given pH. This conversion against Ag/AgCl reference electrode in 1 M KCl solution shows photovoltage and is clarified as below:

$$E\ (V\ \textit{vs.}\ RHE) = E\ (V\ \textit{vs.}\ Ag/AgCl) + E_{Ag/AgCl\ as\ RE}\ (V) + 0.0591 \times pH\ (V) \qquad \text{Eq. S5}$$

$E_{Ag/AgCl}$ = +0.22 V *vs.* (NHE) at 25°C

To benchmark the efficiency of photocatalytic water splitting process, several methods, including solar-to-hydrogen (STH) efficiency[18], have been developed. A requirement for a photocathode to drive water splitting spontaneously is having E_{fb} more positive than oxygen evolution potential (1.23 V *vs.* RHE); however, most cases are not spontaneous and an additional bias is needed to gain a positive potential more than 1.23 V *vs.* RH[18]. Applied bias photon-to-current conversion efficiency (ABPE) method is the method where potential bias (V_b) is applied between working and reference electrodes. It should be mentioned that STH is driven from ABPE equation once the V_b in Eq. 1 is equal to zero under short circuit conditions.

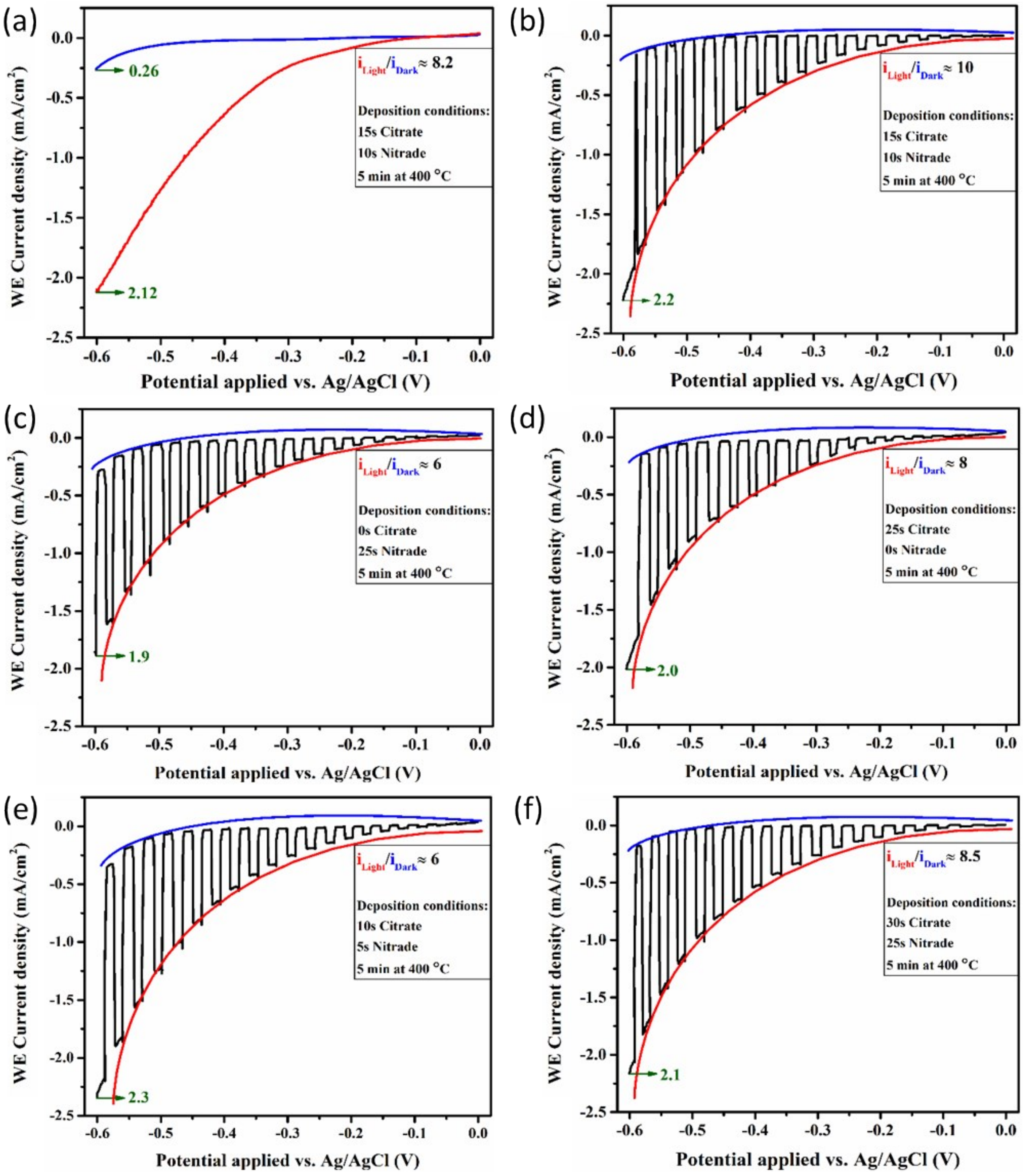

Fig. S10 Photocurrent (j-V) plots of the heat-treated Cu-based ultrathin films in 0.1 M KOH under the scan rate of 10 mV.s^{-1}, the illumination intensity of AM 1.5 G, potential window of 0.0 to -0.6 V *vs.* Ag/AgCl. **(a)** Under continuous illumination; the chopped light at ≈0.5 Hz frequency in deposition condition of **(b)** 15 s in the citrate solution and 10 s in the nitrate solution, **(c)** only 25 s in the nitrate solution, **(d)** only 25 s in the citrate solution, **(e)** 10 s in the citrate solution and 5 s in the nitrate solution, and **(f)** 30 s in the citrate solution and 25 s in the nitrate solution.

In **Fig S11**, the results reveal the photoelectrode possesses p-type conductivity and an open-circuit photovoltage (V_{ph}) of ~0.23 V. The plateau after 300 mW.cm^{-2} means the significant pinning of Fermi level[18].

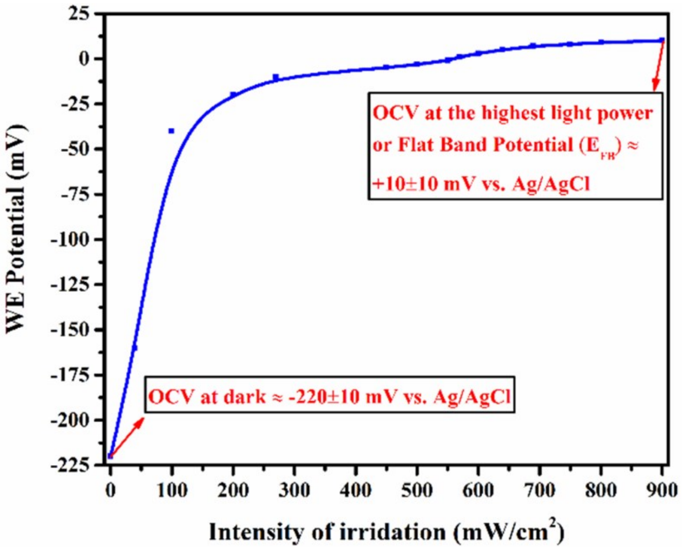

Fig. S11 Open circuit voltage (OCV) from dark to the highest intensity of the Xe lamp.

Photocorrosion stability

One of the most challenging obstacles in the development of PEC semiconductors for solar hydrogen production is photocorrosion in aqueous media. In photocathodes, instead of driving HER, photogenerated holes can oxidise the semiconductor itself and cause unfavourable physical and chemical reactions[18]. In the photocurrent durability test, the current density against time for multiple biases under illumination is plotted, as shown in **Fig. S12**. It is clear that in -0.5 V *vs.* Ag/AgCl, the corrosion rate is significantly higher, leading to a shorter lifespan and performance loss of the film, although the photocurrent density is rather 3 times more than -0.3 V *vs.* Ag/AgCl. It is noteworthy that the curve shape for the stability test depends significantly on the material and system and no specific pattern can be expected[18].

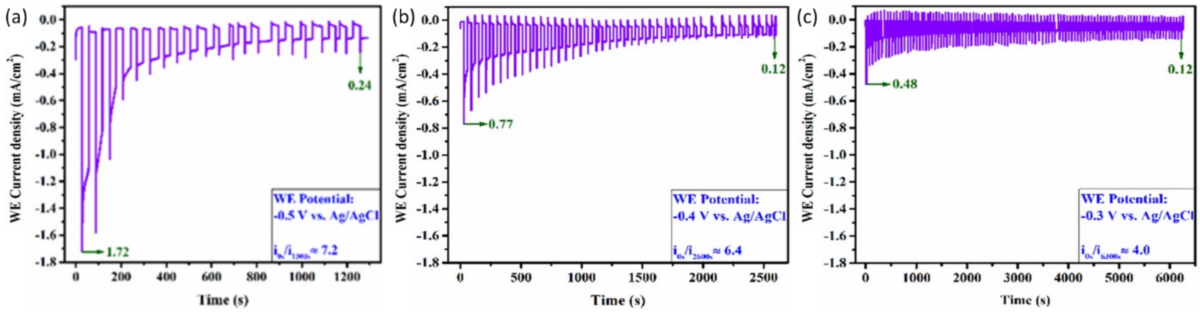

Fig. S12 Photocurrent durability test of the heat-treated trilayered Cu-based ultrathin film in 0.1 M KOH under the illumination intensity of AM 1.5 G, in which the photocurrent *vs.* illumination time is plotted for applied potential of **(a)** -0.5, **(b)** -0.4, and **(c)** -0.3 V *vs.* Ag/AgCl reference electrode.

SUPPLEMENTARY NOTE 4 | LIFE CYCLE ASSESSMENT (LCA)

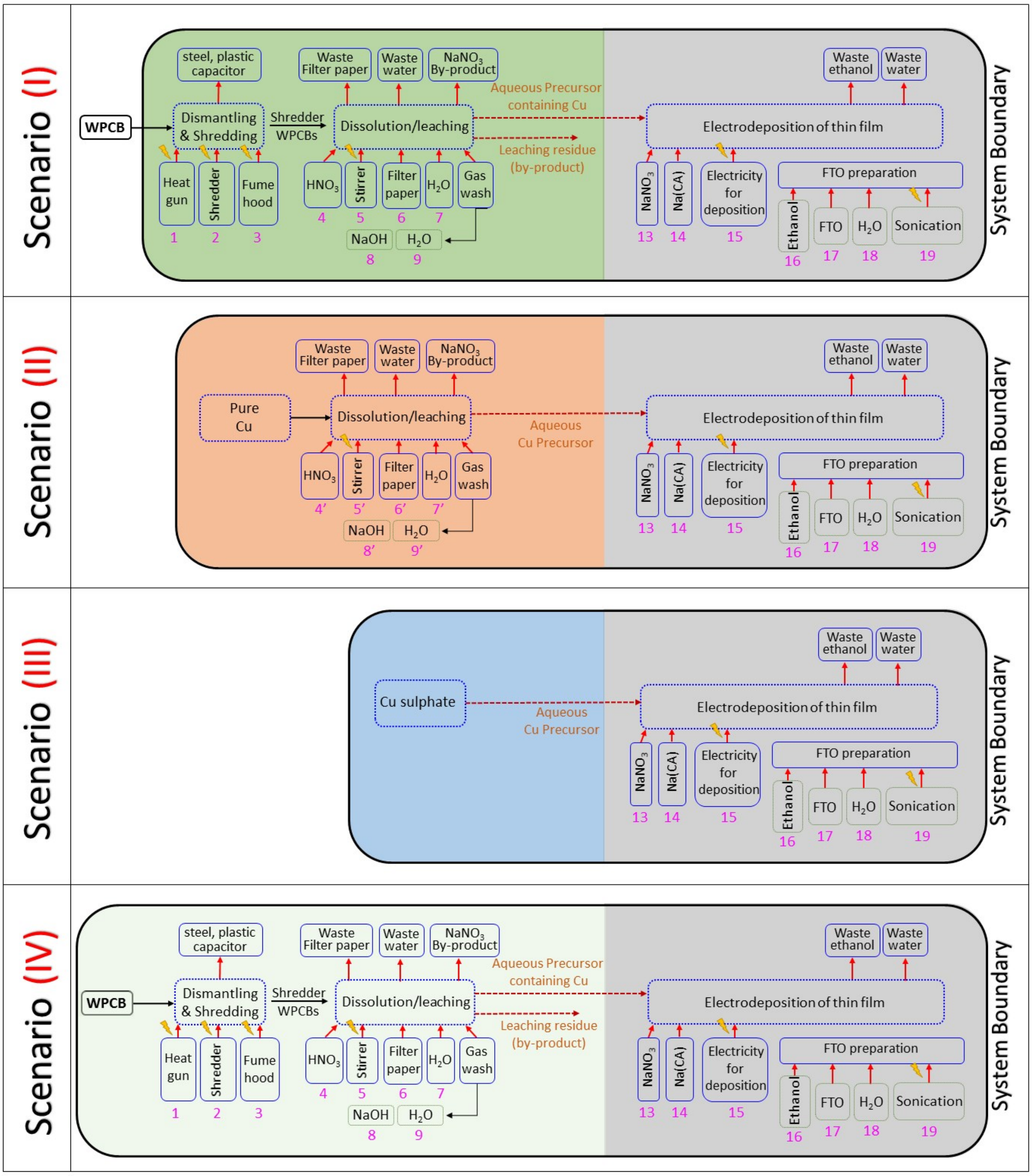

Fig. S13 Details of processes, including the materials, equipment, by-products, and emissions, for four scenarios assumed in the fabrication of the ultrathin film.

Table S1 Life cycle inventory to produce 1 m^2 ultrathin film. Details of materials and energy input/output, emissions, consumption, and unit process of the items for all steps of 3 different Scenarios in this research, extracted from Ecoinvent V.3 inventory in SimaPro V.9. The calculation details of these values are available in **Supplementary Table S2**.

Input/Output	Consumption	Unit	Unit process
Scenario (I): From WPCBs for 1 m^2 of ultrathin film			
Nitric acid 50 wt%	12.753	g	Nitric acid, without water, in 50% solution state {RoW}| market for nitric acid, without water, in 50% solution state | APOS, U
Water	68.826	g	Water, deionised, from tap water, at user {RoW}| market for water, deionised, from tap water, at user | APOS, U
Sodium hydroxide 50 wt%	1.943	g	Sodium hydroxide, without water, in 50% solution state {GLO}| market for | APOS, U
Electricity	1.956	Wh	Electricity, medium voltage {AU}| market for | APOS, U
Process emission			
Wastewater	16.194	g	
process Waste	0.032	g	filter paper waste
Scenario (II): From Pure Cu for 1 m^2 of ultrathin film			
Pure copper	0.896	g	Copper {GLO}| market for | APOS, U
Nitric acid 50 wt%	8.964	g	Nitric acid, without water, in 50% solution state {RoW}| market for nitric acid, without water, in 50% solution state | APOS, U
Water	52.63	g	Water, deionised, from tap water, at user {RoW}| market for water, deionised, from tap water, at user | APOS, U
Sodium hydroxide 50 wt%	1.457	g	Sodium hydroxide, without water, in 50% solution state {GLO}| market for | APOS, U
Electricity	0.081	Wh	Electricity, medium voltage {AU}| market for | APOS, U
Process emission			
Wastewater	4.049	g	
Process waste	0.008	g	filter paper waste
Scenario (III): From Cu sulphate for 1 m^2 of ultrathin film			
Copper sulfate	2.250	g	Copper sulfate {GLO} | market for | APOS, U
Last similar step in all 3 Scenarios: Electrodeposition of Ultrathin Film			
Water	1068.83	g	Water, deionised, from tap water, at user {RoW}| market for

			water, deionised, from tap water, at user | APOS, U
Ethanol	236.70	g	Ethanol, without water, in 95% solution state, from fermentation {GLO}| market for | APOS, U
Sodium nitrate	2.1508	g	Sodium nitrate {GLO}| market for | APOS, U
Citric acid	4.8615	g	Citric acid {GLO}| market for | APOS, U
FTO glass	3920	g	[24]
Electricity	1090.28	Wh	Electricity, medium voltage {AU}| market for | APOS, U
Process emission			
Wastewater	1068.83	g	
Waste ethanol	236.7	g	
Scenario (IV): From WPCBs with avoided Cu extraction impact for 1 m^2 of ultrathin film			
Copper concentrate (containing 28.4% Cu)	3.155	g	Copper concentrate, sulfide ore {GLO}| market for copper concentrate, sulfide ore | APOS, U

Table S2. Detailed table of life cycle inventory to produce 1 m^2 ultrathin film.

Step Number	**Step/Device**	**Comments**	**Usage**	**Reference**
Scenario (I): From WPCBs for 1 m^2 of the ultrathin film; where 1 WPCB can provide 123 g Cu to produce 123 m^2 of ultrathin film Why divided by 123? 24.6 wt% Cu in 500 WPCB provides 123 g Cu The average thickness of the thin films is 150 nm made of Cu oxide or 100 nm made of Cu / The density of Cu is 8.96 g/cm^3 and we assumed that 90% of Cu is extracted[25]				
1	Heat gun	Device power: 2000 Wh Usage time: 4 min	133 W/123	Link
2	Shredder	Device power: 7500 Wh Usage time: 30 s	63 W/123	Link
3	Ventilation/fume hood; for Heat Gun	Device power: 210 Wh Usage time: 4 min	16 W/123	Link
4	Nitric acid 50 wt%	2.0 M at 0.08 solid(g) to liquid(mL) ration final solution: 6.25 L HNO$_3$ molar mass 63 g	1575 g/123	
5	Stirrer	Device power: 60 Wh Usage time: 30 min	30 W/123	Link
6	Filtration using filter paper	4 paper (d=30 cm)	\$2.4/123	Link
7	Washing the residue (water) + water for dilution	1.5 + 5 L = 6500 g	6500 g/123	
8	Sodium hydroxide 50 wt%	Used for gas washing set up: 3 bottles (0.5 L) of 2.0 M NaOH molar mass 40 g	240 g/123	
9	Water for gas washing	2 L = 2000 g	2000	

			g/123	
Scenario (II): From pure Cu for 1 m^2 of the ultrathin film; where 123 g Cu is taken to produce 123 m^2 of ultrathin film				
4´	Nitric acid 50 wt%	123 g Cu from WPCB needs 553.5 g HNO_3 100 wt% Cu molar mass: 63 g	1107 g/123	
5´	Stirrer	Device powder: 20 Wh Usage time: 30 min	10 W/123	Link
6´	Filtration using filter paper	1 paper (d=30 cm)	$0.6/123	Link
7´	Water usage	5 L = 5000 g	5000 g/123	
8´	Sodium hydroxide 50 wt%	Used for gas washing set up: 3 bottles (0.5 L) of 1.5 M NaOH molar mass 40 g	180 g/123	
9´	Water for gas washing	1.5 L = 1500 g	1500 g/123	
Scenario (III): From Cu sulphate for 1 m^2 of the ultrathin film; where 276.75 g Cu sulphate is taken to produce 123 m^2 ultrathin film				
Scenario (IV): From WPCBs with avoided Cu extraction impact for 1 m^2 of ultrathin film; where 3.155 g Cu concentrate is taken to produce 1 m^2 ultrathin film				
Last similar step in all 3 Scenarios: Electrodeposition of ultrathin film				
13	Sodium nitrate (1 M)	31.25 L diluted leaching solution (1/10) NaNO3 molar mass: 85 g/cm^3	2657 g/123	
14	Citric acid (instead of sodium citrate, due to lack of inventory) (1M)	31.25 L diluted leaching solution (1/10) Citric acid molar mass: 192.2 g/cm^3	6004 g/123	
15	Electricity for deposition (calculated)		111500 W/123	Link
16	Water usage (dilution and replacement (8.5 L), and FTO cleaning (123.5L))	132 L = 132000 g	132000 g/123	
17	Cleaning the FTO (ethanol)	1 m^2 ultrathin film uses 300 mL Ethanol density: 0.789 g/mL	236.7 g	
18	FTO glass (made inventory)	1 m^2 ultrathin needs 5.04 kg FTO glass	5040 g	*[24]
19	Sonication process	Device power: 600 W Usage time: 5 × 20 min	1000 W	Link

*Inventory of the FTO glass was extracted from the ref.[24].

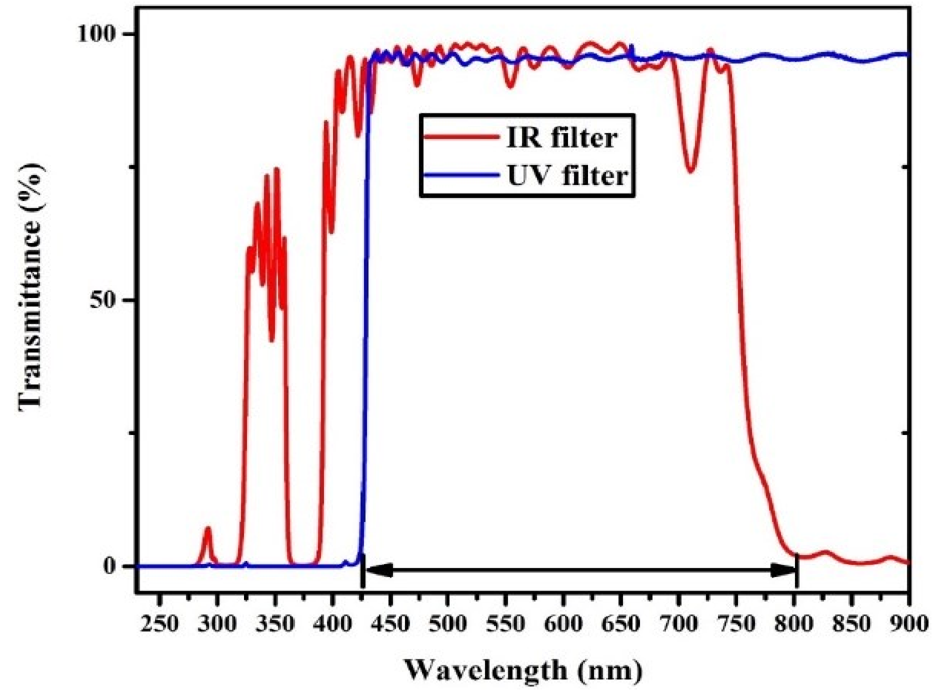

Fig. S14 UV-Vis spectrum of IR and UV filters assembled on a xenon lamp for water splitting application.

References

1 S. Shin, C. Park, C. Kim, Y. Kim, S. Park and J. H. Lee, *Curr. Appl. Phys.*, 2016, **16**, 207–210.

2 C. Oulmas, S. Mameri, D. Boughrara, A. Kadri, J. Delhalle, Z. Mekhalif and B. Benfedda, *Heliyon*, 2019, **5**, e02058.

3 E. Chassaing, K. Vu Quang and R. Wiart, *J. Appl. Electrochem.*, 1986, **16**, 591–604.

4 Z. Zhang and P. Wang, *J. Mater. Chem.*, 2012, **22**, 2456–2464.

5 Z. Mezine, A. Kadri, L. Hamadou, N. Benbrahim and A. Chaouchi, *J. Electroanal. Chem.*, 2018, **817**, 36–47.

6 Database of X'pert Analytica Software.

7 R. A. Ball and A. S. Malin, *Aust. Gemol.*, 1973, **11**, 16–19.

8 Y. J. Jang, J. W. Jang, S. H. Choi, J. Y. Kim, J. H. Kim, D. H. Youn, W. Y. Kim, S. Han and J. Sung Lee, *Nanoscale*, 2015, **7**, 7624–7631.

9 L. V. Devi, T. Selvalakshmi, S. Sellaiyan, A. Uedono, K. Sivaji and S. Sankar, *J. Alloys Compd.*, 2017, **709**, 496–504.

10 D. Marrocchelli, S. R. Bishop, H. L. Tuller and B. Yildiz, *Adv. Funct. Mater.*, 2012, **22**, 1958–1965.

11 J. Y. Kim, J. A. Rodriguez, J. C. Hanson, A. I. Frenkel and P. L. Lee, *J. Am. Chem. Soc.*, 2003, **125**, 10684–10692.

12 J. E. Bailey, *P. Sciences*, 1964, **279**, 395–412.

13 S. Z. Pu, C. Guo, M. Y. Li, Z. L. Chen and H. M. Zou, *Chinese Phys. B*, 2015, **24**, 046101-046106.

14 Y. He, B. Li, C. Wang and S. X. Mao, *Nat. Commun.*, 2020, **11**, 1–8.

15 S. S. Mofarah, R. K. Nekouei, S. Maroufi, S. Biswal, S. Lim, Y. Yao and V. Sahajwalla, Nanoscale, 2021, Accepted manuscript.

16 J. Su, G. D. Li, X. H. Li and J. S. Chen, *Adv. Sci.*, 2019, **6**, 1–19.

17 Z. Wang, L. Zhang, T. U. Schülli, Y. Bai, S. A. Monny, A. Du and L. Wang, *Angew. Chemie*, 2019, **131**, 17768–17773.

18 Z. Chen, H. N. Dinh and E. Miller, *Photoelectrochemical water splitting: standards, experimental methods, and protocols*, 2013.

19 Y. Yang, D. Xu, Q. Wu and P. Diao, *Sci. Rep.*, 2016, **6**, 1–13.

20 Q. Wang, Y. Zhang, J. Xiao, H. Jiang, T. Hu and C. Meng, *J. Alloys Compd.*, 2019, **782**, 1103–1113.

21 S. Zhang and N. Pan, *Adv. Energy Mater.*, 2015, **5**, 1–19.

22 S. Maroufi, R. Khayyam Nekouei and V. Sahajwalla, *Electrochim. Acta*, 2019, 328, 135061-135070 .

23 G. V. Govindaraju, G. P. Wheeler, D. Lee and K. S. Choi, *Chem. Mater.*, 2017, **29**, 355–370.

24 J. Gong, S. B. Darling and F. You, *Energy Environ. Sci.*, 2015, **8**, 1953–1968.

25 P. M. Hannula, M. K. Khalid, D. Janas, K. Yliniemi and M. Lundström, *J. Clean. Prod.*, 2019, **207**, 1033–1039.